University of Southern California (USC)

Viterbi School of Engineering

Department of Aerospace and Mechanical Engineering

Final Report on Experiments on the Permeability of Anisotropic Porous Structures for Drag Reduction

---

Wednesday December 11th, 2024

AME – 441: Senior Projects Laboratory

Group # 26: Duke Bristow, Gianna Canto, Antoine Moats, and Joe Rees

Primary Advisor: Emma Singer

Secondary Advisor: Mitul Luhar

Direct numerical studies conducted by Gomez et al. (2019) have shown that porous materials with certain permeabilities and anisotropic ratios have the ability to reduce skin friction drag by an estimated 20-25 percent. However, due to the emerging nature of the topic, existing literature has only scratched the surface of the possible design space. Previous experimental studies conducted by Vijay et al. (2023) and Morimoto (2022) have yielded inconclusive results on the effect of anisotropy on drag reduction. This is due to differing experimental and manufacturing techniques as well as the investigation of dissimilar geometries. The goal of this effort is to provide a consistent approach across a range of geometries previously used in the literature, in addition to conducting experiments on two completely new geometries. By conducting pressure drop measurements over cubic, gyroid, riblet, and elliptical geometries, the effect of permeability anisotropy on drag reduction is characterized for Reynolds numbers [500, 3000]. These experiments corroborated past experiments demonstrating streamwise, wall-normal, and spanwise permeabilities of 0.07±0.03, 0.05±0.03, 0.05±0.03 for the cubic geometry as well as 0.22±0.03, 0.009±0.002, 0.061±0.02 for the riblet, 0.05±0.03, 0.027±0.008, 0.027±0.008 for the elliptical and 0.06±0.01, 0.007±0.001, 0.018±0.002 for the gyroid. Despite the high anisotropy of the gyroid and riblet geometries, friction coefficients less than those of a smooth wall were not found. An explanation is proposed for the lack of drag reduction based on arguments by Gomez et al. (2019) demonstrating the existence of Kelvin-Helmholtz (KH) vortices along certain directions. While KH vortices are not suppressed it all directions, it is shown that the gyroid and riblet geometries suppress vortices in at least one direction, demonstrating the need for further experimentation on the design space of these geometries.

Introduction

In recent years, commercial airline and defense agencies have emerged as the key stakeholders in friction-based drag reduction research. Considering flight in cruise conditions, skin-friction drag contributes about half of the total drag, meaning marginal drag reductions can drastically reduce cost, fuel usage, and pollution (Ricco 2021). Further research estimates that reducing drag on aircraft by 1% may lead to a 0.5-1% reduction in fuel consumption depending on the aircraft (Mubarak 2013). Motivated by these goals, past research on friction-based drag has focused on both passive methods, such as shark skin-inspired riblets and hydrophobic coatings, and active methods including rotating wall boundaries and plasma-producing electrodes (Ricco 2021). Though active methods have higher theoretical drag reduction capabilities, passive methods are much cheaper, easier to implement, and require no power (Fu 2017). Passive methods for friction-based drag reduction have emerged as a promising field of study; drawing inspiration from biology, research on passive drag reduction has found that the jaggedness of shark scales reduces circular flow along the surface leading to a decrease in friction. This discovery has led to numerous experimental and computational studies on surface roughness and drag reduction as well as the implementation of riblets, or microscopic grooves, on the surface of airplane wings.

The simulated and experimental success of riblet geometries has motivated researchers to characterize the maximum possible drag reduction of a wide range of surface topologies. Direct numerical studies of riblet geometries have found that the maximum drag reduction is approximately 10 percent, which in practice, decreases by a factor of 4 due to Reynolds scaling (Fu 2017). Current research attributes the maximum efficacy of riblets to the development of Kelvin-Helmholtz (KH) vortices (spiraling fluid motion) in the spanwise and wall-normal directions as the Reynolds number increases. To mitigate the formation of KH vortices in the spanwise and wall-normal directions, researchers have investigated a type of anisotropic porous structure, called streamwise preferential porous structures (Morimoto 2022). These structures provide different flow resistances in the streamwise, wall-normal, and spanwise directions ideally reducing KH vortices, leading to laminar flow along the wall boundary. Motivated by these unique structures, Gomez et al. (2019) sought to demonstrate the maximum drag reduction of anisotropic porous structures using direct numerical simulations. They found that porous structures with certain permeabilities may cause 20-25 percent drag reduction illustrating a twofold increase in drag reduction compared to riblets.

Currently, no studies have been published detailing how the permeabilities specified by Gomez et al. (2019) can be experimentally achieved. This experiment aims to fill this gap. One study conducted by Vijay et al. (2023) sought to attain these permeabilities using cubic streamwise preferential porous structures with varying Bravais-lattice vectors. This study did not achieve drag reduction due to unsatisfactory permeability values. However, it provides a good foundation for this investigation, which seeks to explore the effect of various cell geometries and pore sizes on permeability and drag reduction. To properly investigate the impact of cell geometries and pore size on permeability, pressure drop measurements along 3D-printed porous structures will be used to calculate the permeability and skin friction coefficient.

Theory & Basic Equations

Once each geometry is 3D printed, the permeability and anisotropic ratios will be determined using pressure drop measurements for each dimension shown below in Fig. 1.

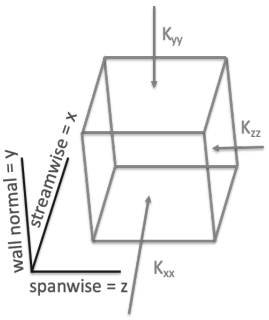

Figure 1. Diagram highlighting the direction of flow and relationship between permeability variables.

Anisotropic ratios are a dimensionless quantity used to specify how preferential the structure is in a certain direction and is defined as follows:

$$\phi_{xy} = \frac{k_{xx}}{k_{yy}} \qquad \text{Equation 1}$$

where k_{xx} is the permeability in the x-direction and k_{yy} is the permeability in the y-direction etc. The permeability will be determined experimentally, measuring the pressure drop and volumetric flow rate of a fluid flowing through the porous geometry in a permeability chamber, as shown in Figure 2.

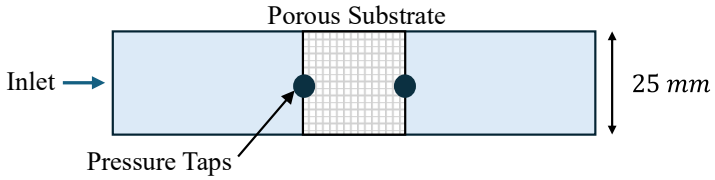

Figure 2. Permeability chamber used to calculate the permeability using Forchheimer's correction to Darcy's Law, outlined in Equation 2.

After determining the pressure gradient across the porous medium, its permeability will be calculated in each direction using Forchheimer's correction to Darcy's law, where the pressure gradient along the boundary in the direction of the flow is not only inversely proportional to the permeability but to higher-order terms as well. At high velocities, the second-order term becomes dominant resulting in an added term to Darcy's equation:

$$\frac{dP}{dx} = \frac{v}{k_{xx}} U_b + C U_b^2 \qquad \text{Equation 2}$$

where v is the dynamic viscosity of the fluid, k_{xx} is the permeability in the x-direction, $\frac{dP}{dx}$ is the pressure drop across the substrate sample, and U_b is the bulk velocity. Pressure drop measurements will also be utilized to calculate skin friction drag reduction using the benchtop water channel shown in Figure 3.

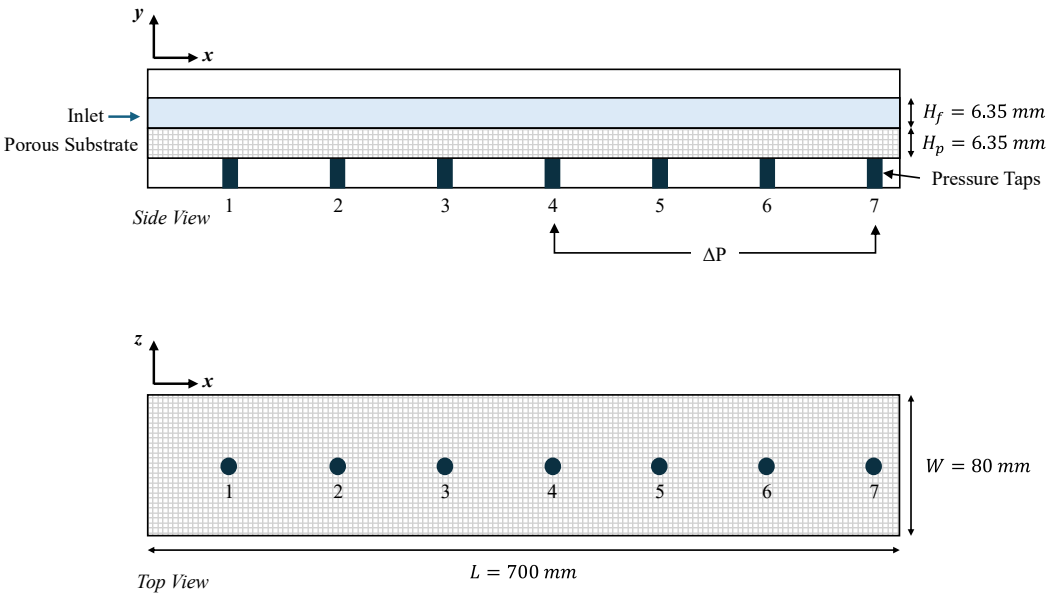

Figure 3: Pressure drop measurements taken from this benchtop water channel will be used to calculate the friction factor using Equation 2.

This is rooted in the concept that the frictional force is proportional to the Darcy friction coefficient. For a rectangular surface, the Darcy friction coefficient is related to the pressure gradient in the following manner:

$$f = \frac{dP}{dx}\frac{2H_f}{\rho U_b^2} \qquad \text{Equation 3}$$

pressure drop measurements within the fully developed flow ($\frac{dP}{dx}$) can be converted into friction factor estimates considering the height of the unobstructed channel (H_f), the density of the medium (ρ), and the bulk velocity of the unobstructed flow (U_b^2).

The exact flow physics governing drag reduction is a current field of research. However, the theory behind the drag reduction of streamwise preferential porous structures is rooted in the mitigation of vortices along the solid-fluid boundary. One pivotal difference between riblets and streamwise preferential porous structures is that in riblets there is no flow resistance in the wall-normal direction while in porous structures there is. In theory, for porous structures, the flow resistance in the wall-normal direction limits the formation of KH vortices in the wall-normal direction (Gomez et al. 2019). However, the suppression of KH vortices in both the spanwise and wall-normal direction is dependent on the permeability in each direction which is dictated by pore size and geometry. Gomez et al. (2019) also identified the normalized permeability as a dimensionless parameter that dictates the suppression of KH vortices.

$$\sqrt{K_{yy}^{+}} = \frac{\sqrt{K_{yy}}u}{v} \qquad \text{Equation 4}$$

where k_{xx} is the permeability in the y-direction, v is the kinematic viscosity, and u the unobstructed flow velocity determined from $2pu = -\frac{dp}{dx}H_f$.

Experimental Technique

Geometry Design

Manufacturing capabilities and printer resolution outlined in (Vijay et. al. 2023) established limitations on the minimum scale of the geometries (0.4 mm). Based on experiments of cubic geometries, structures with large anisotropy ratios ($\phi_{xy} > 1.0$), small pore sizes in the streamwise direction (0.4mm), and large pore size in the wall-normal and spanwise direction (3 mm) did not reduce drag but performed the best compared to structures with smaller anisotropy ratios.

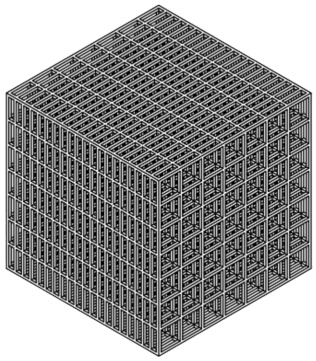

Figure 4. Cubic porous geometry informed by the findings of Vijay et al. (2023).

As a result, the current experiment will keep similar pore sizing of ~0.4 to 3mm but utilize different geometries: elliptical/circular pores, gyroid pores, and permeable riblets. No experiments have been conducted utilizing elliptical and gyroid geometries and direct numerical simulations demand extensive expertise and resources, so quantitative predictions are currently impossible. Additionally, a multi-layered trapezoidal riblet geometry was created, inspired by the steel mesh stacked riblets designed by Morimoto and Suga (2022).

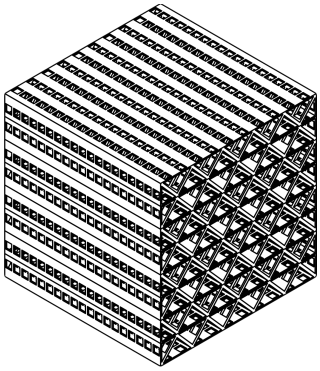

Figure 5. Multi-layer trapezoidal riblet, inspired by experiments conducted by Morimoto and Suga (2022).

Studies by Morimoto (2022) illustrated that permeable, multi-layered riblets of 0.15mm, 0.1mm, 2.5mm dimensions performed just as well as a smooth wall (Morimoto 2022). Due to the minimal resolution of the 3D printer, the pore sizing of the riblet geometry tested will be slightly larger ~0.4 mm. The elliptical design, inspired by previous experimental cubic pore sizes, incorporated rows of ellipses with constant radii in the x (5.5 mm), y, and z directions (semi-minor = 0.4 mm, semi-major = 2.48 mm).

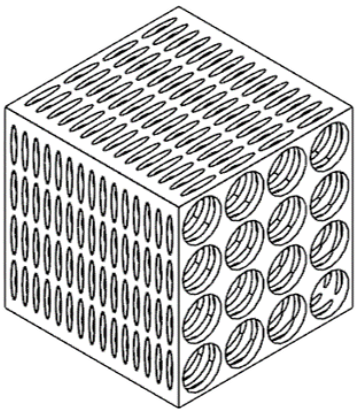

Figure 6. Elliptical geometry designed with similar pore sizing as the cubic geometry.

This structure was chosen because curved geometries tend to result in smoother flow profiles, reducing the velocity gradient of the flow and subsequently the frictional forces resulting in turbulence. Like the elliptical case, the gyroid lattice structure was selected because of its smooth surfaces.

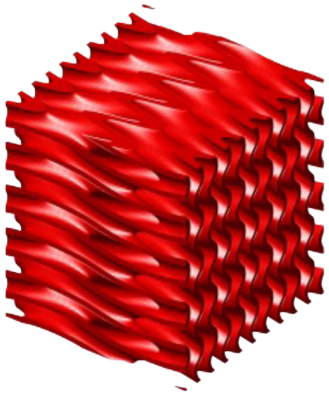

Figure 7. Gyroid geometry design inspired by bone growth studies conducted by Zhao et al. (2021)

In addition to the smooth surfaces along the boundaries, gyroid geometries have been shown to be very structurally sound (Zhao et al. 2021). This kind of strength is important since aircraft fly at Reynolds numbers in the order of 10^6 and greater, and as the velocity of the flow increases, the stress on the pores increases. This is a key concern for many riblet geometries with sharp features, as they have been shown to fail under certain flow conditions. The gyroid's unique geometry is determined by the gyroid surface approximation shown in Equation 4.

$$\sin(x)\cos(y) + \sin(y)\cos(z) + \sin(z)\cos(x) \qquad \text{Equation 5}$$

Using scaled coefficients associated with x,y, and z the pore sizing in each direction can be altered. This is important to note as future experiments will entail a geometric parameter sweep of varying pore sizing. In addition, skin friction measurements were conducted with two different sponges to explore the difference in behavior between structured and unstructured porous geometries.

Data Acquisition and Experimental Procedure

Porous substrates with elliptical, gyroid, and riblet-based geometries were printed using a Formlabs Form3 and Prusa SL1S Resin SLA printers and tested in both a permeability chamber and benchtop channel flow setup. The benchtop water channel shown in Figure 8 was designed by Vijay et al. (2023) to measure the pressure drop across the fully developed region of an unobstructed flow, configured as shown in Figure 8 with a total length, L, of 700 mm and a total width, W, of 80 mm.

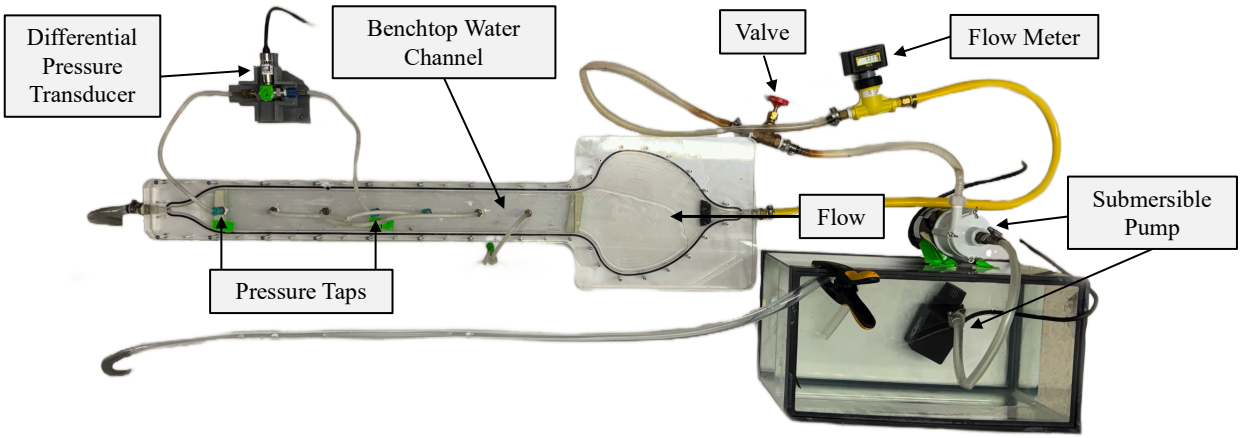

Figure 8. Working benchtop water channel setup.

For each porous substrate, multiple evenly sized plates of height, H_p, were flush mounted within the benchtop water channel, where a submersible pump (Little Giant 503103) generated a flow within an unobstructed portion of the channel with height H_f, parallel to the substrate. Seven evenly spaced pressure taps are arranged along the test section's centerline, where a wet-wet high-resolution differential pressure transducer with an accuracy of ± 0.08% BSL (Omega PX-409) measured the pressure drop across pressure taps 4 and 7. The region between taps 4 and 7 is where Vijay et al. (2023) were able to identify fully developed flow, where the pressure decreased linearly with distance.

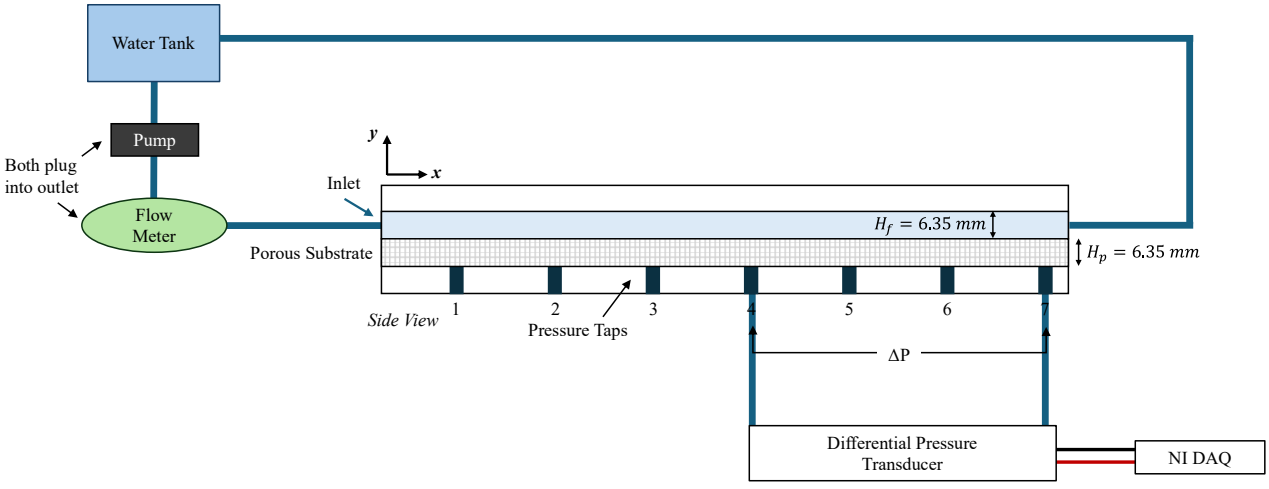

Figure 9. Schematic of the benchtop water channel, including the water tank, pump, flow meter, differential pressure transducer, and National Instruments DAQ.

As shown in Figure 9, the differential pressure transducer was connected to a National Instruments USB Multifunction DAQ, which powers the pressure transducer with a 10 V excitation voltage. A MATLAB script was used to collect the voltage difference measurements with a sampling rate of 1650 samples per second and a sampling time of 100 seconds. Voltage difference measurements were recorded at incremental flow rates between 0 and 3.8 GPM, monitored by a flowmeter (Blue-White Industries RB-100PI-GPM2) attached to the channel's inlet pipe. Four trials were conducted for each geometry. The permeability of each porous substrate was measured experimentally using the permeameter setup designed by Vijay et al. (2023), shown in Figure 10.

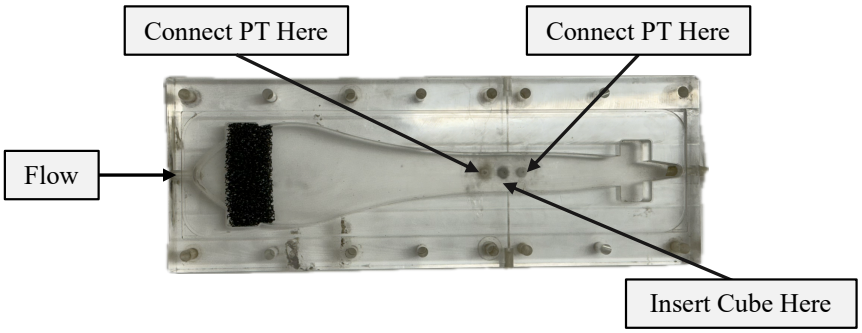

Figure 10. Working permeability chamber.

For testing in the permeability chamber, each substrate was 3D-printed as a cube with a 25 mm side length. The cubes were fitted in a square duct, where a submersible pump drove a regulated flow across each sample, and the PX-409 pressure transducer recorded the pressure difference across the substrate.

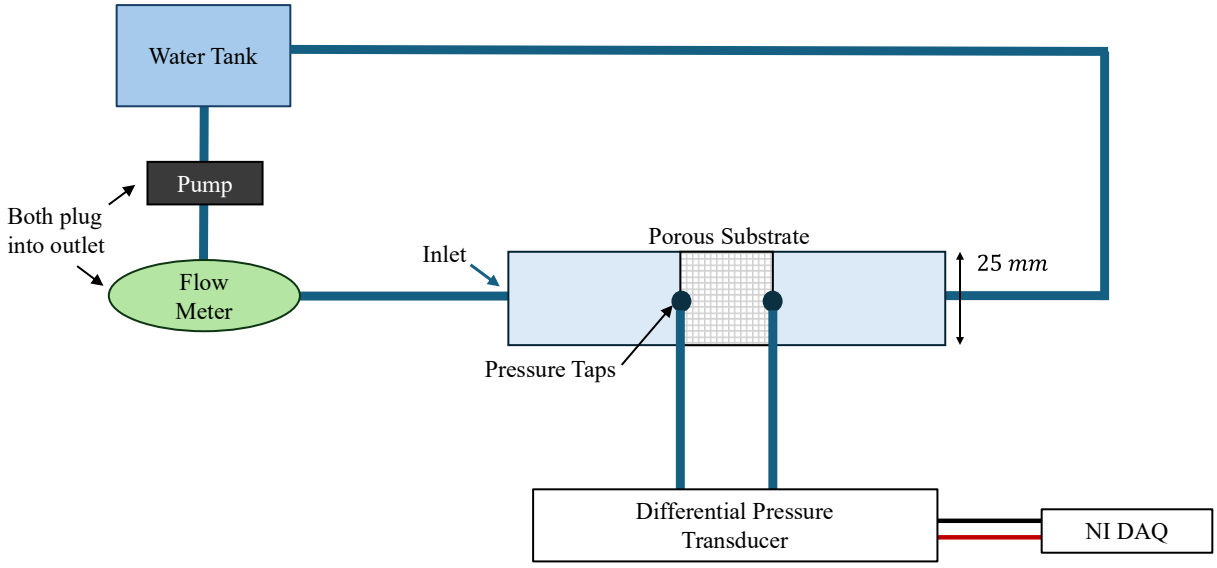

Figure 11. Schematic for permeability setup including the same water tank, pump, flow meter, differential pressure transducer, and National Instruments DAQ used for the benchtop measurement.

As shown above in Figure 11, the permeability setup utilized a similar experimental procedure as the benchtop water channel, making use of the same submersible pump, water tank, flow meter, pressure transducer, DAQ, and MATLAB script. For each geometry, the voltage difference was

recorded for flow rates between 0 and 0.600 GPM at 0.100 increments. The procedure was repeated for multiple trials across all directions.

Results

For both the benchtop and permeability measurements, voltage differences were normalized for each recorded trial to eliminate the noise across each trial. Because the Omega PX-409 differential pressure transducer (PT) produces voltage difference measurements in mV/V, a calibration constant was experimentally derived to convert these measurements into pressure measurements, used to determine the pressure gradient in Pascals/meter. To achieve this, two tubes were attached to either end of the PT and filled with water. The hydrostatic pressure equation was used to measure the pressure in the tubes such that

$$P = \rho g h \qquad \text{Equation 6}$$

where h is the measured height difference between the columns of water in the tube, g is the acceleration due to Earth's gravity and ρ is the density of the water. The height of the water in the tubes was measured by using a measuring tape. The uncertainty of the height measurement was determined based on the resolution of the measuring tape. Additionally, the uncertainty of the voltage output measured was determined based on the resolution of the PT. The PT's output voltage was plotted against the calculated expected pressure based on the hydrostatic equation and is shown below in Figure 12.

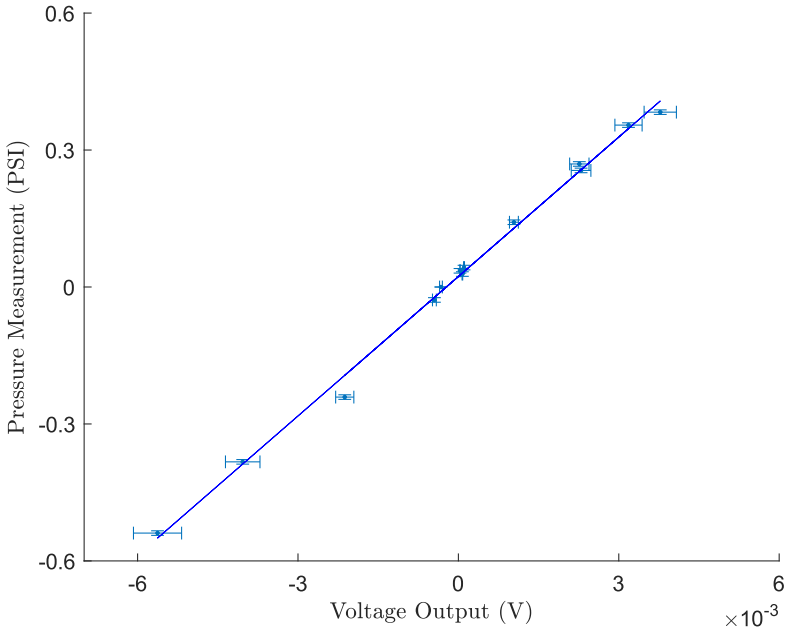

Figure 12. Calibration curve for PT converting from voltage to pressure

As shown above in Figure 12, there is a linear relationship between the output voltage of the PT and the corresponding expected pressure as determined through use of the hydrostatic equation. The calibration constant for the PT was within 2% of the calibration constant as measured

by previous experiments using the same device (Vijay 2023). This calibration constant was used to convert from output voltage (mV/V) to pressure (PSI), measured to be 101.82 $\pm$ 0.064. The uncertainty for this calibration constant was determined using the R^2 value from the graph shown in Figure 12. The uncertainty for the voltage measurement was determined based on the specifications from the manual of the pressure transducer (Omega 2024). The uncertainty of the corresponding PSI measurement was based on the resolution of the ruler used to measure the height of the water.

Using this calibration constant, the pressure drop across each geometries was measured. By manipulating Equation 2, the measured pressure gradient and bulk velocity were used to calculate the permeability of each geometry. Cubes were placed in the permeability chamber and rotated to measure the permeability of the geometries in all directions.

Table 1: Permeability values for the streamwise, K_{xx}, wall-normal K_{yy}, and spanwise, K_{zz}, directions as well as the anisotropy ratios (ϕ) for the geometries conducted. The cubic geometry permeability ratios concluded from previous experiments.

Geometry	$K_{xx}(mm^2)$	$K_{yy}(mm^2)$	$K_{zz}(mm^2)$	ϕ_{xy}	ϕ_{yz}	ϕ_{xz}
Trapezoidal Riblets	0.22 ± 0.03	0.009 ± 0.002	0.061 ± 0.02	28 ± 10	0.3 ± 0.3	1.2 ± 0.2
Gyroid	0.06 ± 0.01	0.007 ± 0.001	0.018 ± 0.002	8 ± 2	0.4 ± 0.1	3.4 ± 0.7
Cubic	0.07 ± 0.03	0.05 ±0.03	0.05 ± 0.03	3 ± 2	2 ± 1	3 ± 2
Elliptical	0.05 ± 0.03	0.027 ± 0.008	0.027 ± 0.008	2 ± 1	1 ± 0.6	2 ± 1
Previous Experiments						
Cubic (Vijay 2023)	0.07 ± 0.01	0.07 ± 0.01	0.07 ± 0.01	1 ± 0.3	1 ± 0.3	1 ± 0.3

As shown in Table 1, the permeability measurements for the cubic geometry are equal to those of previous studies. This correlation ensures the PT is functioning correctly. The pressure drop measurement and bulk velocity are plotted below to highlight the difference in performance of the riblet and elliptical geometries.

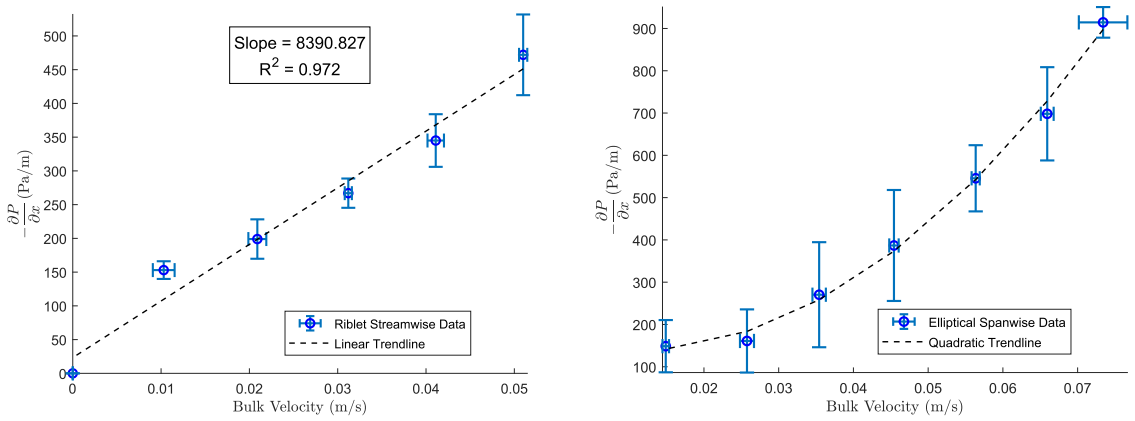

Figure 13. Comparison between riblet and elliptical geometries

As shown in Figure 13, there is a linear relationship between bulk velocity and pressure drop for the riblet geometry in the streamwise direction. However, there is a quadratic relationship between bulk velocity and pressure drop for the elliptical in the spanwise direction. Once the permeability of each geometry was characterized, skin friction profiles were measured. The relationship between friction factor and Reynolds number is shown below in Figure 14.

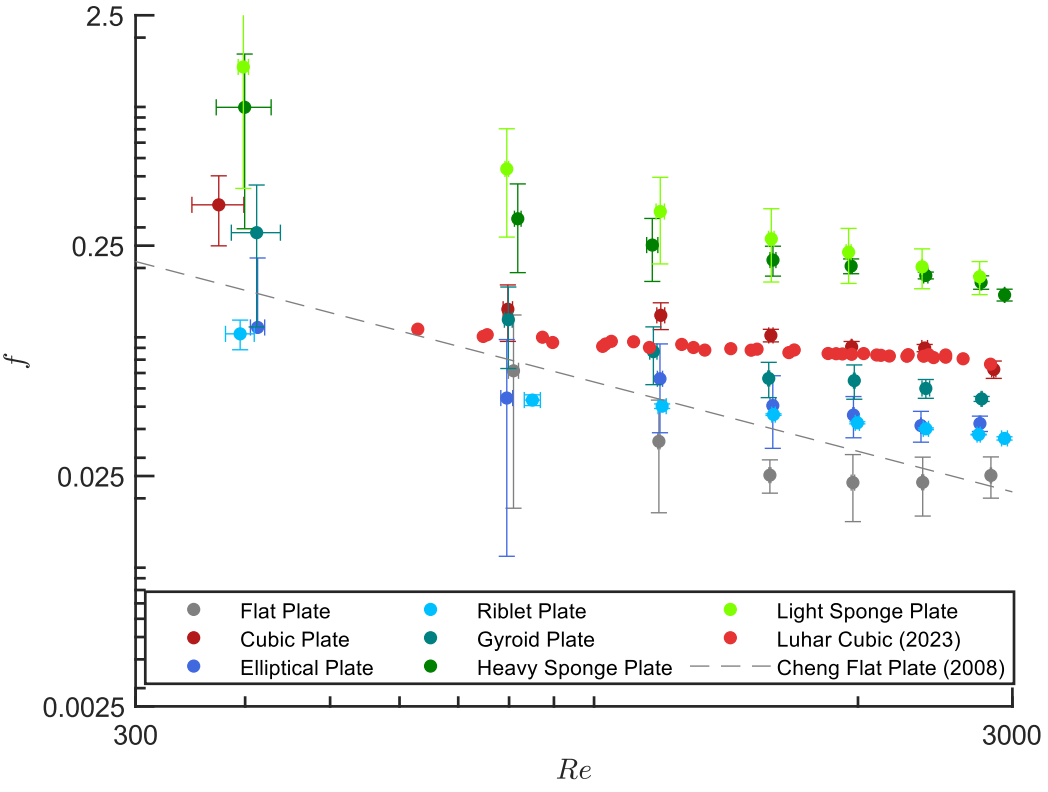

Figure 14. Correlation between friction factor and Reynolds number for different geometries

As shown above, in Figure 14 the measurements collected using the flat plate line up with expected flat plate performance as predicted by Cheng (2008), validating the experimental setup.

Discussion

As presented in Figure 14, the elliptical, multi-layered riblet, and gyroid all performed better compared to the cubic structure. Furthermore, cubic data collected by Vijay (2023) stabilized around a Reynolds number of 1750 and a skin friction drag coefficient of 0.1 while current experiments did not stabilize. Comparing the skin friction performance of the different geometries to pore sizing does not illustrate a consistent trend. The elliptical geometry had large differences in the streamwise and spanwise pore sizes while the gyroid geometry did not. Yet, the gyroid and elliptical geometries' skin friction profiles were similar. These observations corroborate previous experiments demonstrating that pore sizing should not be the only metric used to alter skin friction coefficients. The other important metric that has been shown to impact skin friction coefficients is the permeability and permeability ratios. Based on previous experiments and simulations, it is expected that the geometries with the highest streamwise to wall-normal permeability ratios will perform the best. However, as noted in Table 1, the elliptical geometry did not have a large anisotropy ratio (ϕ_{xy}), but yielded similar results to the geometries that did.

Previous literature highlighted that large anisotropy ratios (ϕ_{xy}) would produce the best results given the symmetry condition that $\phi_{yz} = 1$ (i.e. $\frac{K_{yy}}{K_{zz}} = 1$). As presented in Table 1, this criteria was only true for the elliptical and cubic structures. For these structures, a greater anisotropy($\phi_{xy} > 1$) did result in lower skin friction profiles, illustrating that, under the symmetry condition, greater anisotropy is conducive to reducing skin friction coefficients. Future studies should focus on balancing these structures to meet the symmetry condition to see further improvements in skin friction drag reduction. In addition, skin friction measurements were also conducted for two different sponge types: heavy-duty and no-scratch. The results of these two unstructured geometries shown in Figure 14 were poor, causing further comparison on the permeability ratios to be unjustified.

The lack of drag reduction for all the geometries can be attributed to the relatively high normalized permeabilities. According to Gomez et al. (2019) the normalized permeability must be equal to or less than 0.4 for the suppression of KH vortices in the wall-normal and spanwise directions. While similar results were obtained from previous experiments conducted by Vijay (2023), the gyroid and riblet geometries were found to satisfy this criteria for Reynolds numbers < 2500. Shown below in Figure 15, the normalized wall-normal permeabilities of each geometry are plotted with respect to Reynolds number, illustrating the regimes where the normalized wall-normal permeability criteria is met. Unsurprisingly, the cubic geometry never meets this criteria, corroborating the poor performance of the skin friction coefficient. However, the gyroid and riblet geometries met this condition for Reynolds numbers below 2000 which coincides with the region where friction factor of the smooth plate and geometries are the closes.

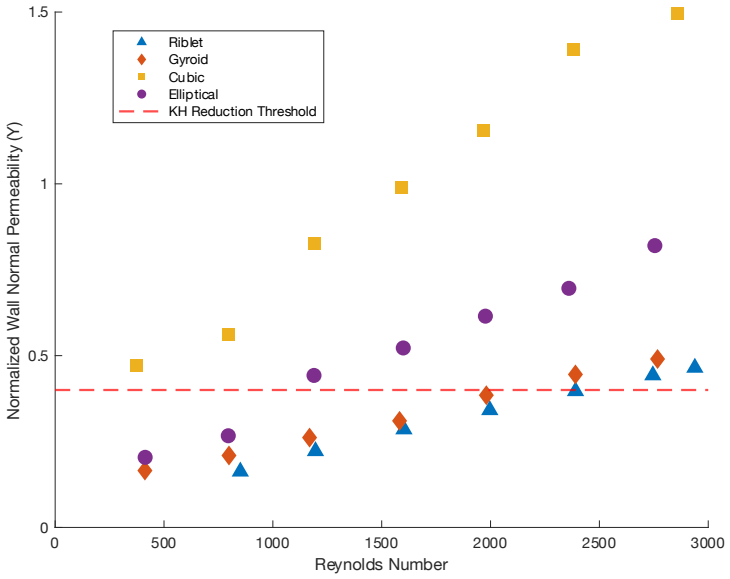

Figure 15. The ability of the gyroid and riblets to reduce vortices in the wall-normal direction for relatively high Reynolds numbers illustrates why they should be further studied.

The fact that the riblet and gyroid geometries do not result in drag reduction can be explained because these structures do not reduce KH vortices in the spanwise directions for Reynolds numbers above ~750.

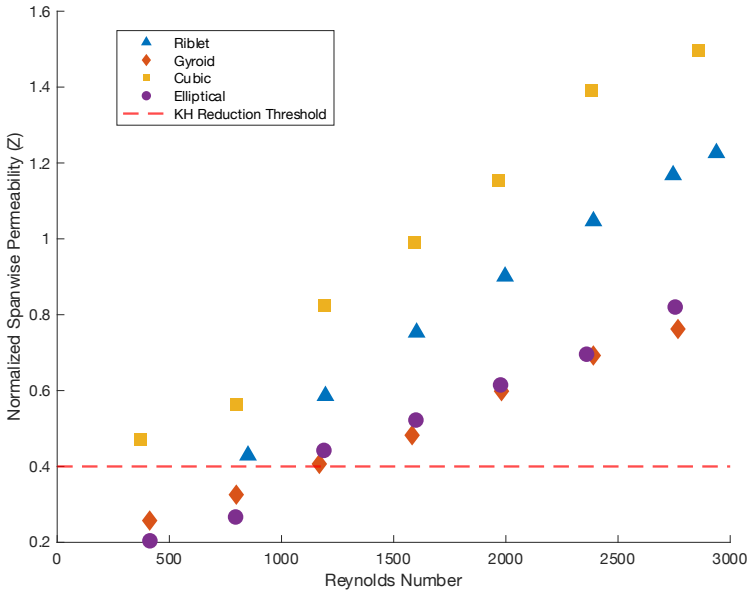

Figure 16. The increase in the normalized wall-normal permeability with respect to Reynolds number is expected for all geometries due to the increase in the pressure gradient as the velocity increases.

The ability of the riblet and gyroid geometries to reduce vortices in one direction while not reducing vortices in another stresses the importance of ensuring that $\phi_{yz} = 1$, a key

assumption of the numerical studies conducted by Gomez et. al. Under this condition, a geometry either suppresses vortices in both directions or none, making it easier to conclude whether the geometry is capable of reducing drag. However, it is evident that if these complex geometries are able to meet the criteria to reduce KH vortices in one direction, they should be able to reduce KH vortices in multiple directions.

Conclusion

This project contains one of the few friction factor and permeability datasets for easily manufactured (3D printed) porous materials. Based on previous experiments and numerical studies, porous materials with streamwise preferential permeabilities may lead to skin friction coefficients lower than those of a smooth wall. Conclusions on the ability anisotropic materials to reduce drag from numerical studies are based on the idealized Darcy-Brinkman equation in the porous medium. Previous experimental studies motivated by these results have yielded differing results. Experiments on riblet geometries have demonstrated that streamwise preferential geometries did not result in drag reduction (Morimoto 2022). However, these measurements were inferred from Reynolds shear stress measurements and were not corroborated by direct pressure drop measurements. Other experiments using pressure drop experiments concluded that high anisotropy may be conducive to drag reduction based on a parameter sweep of cubic geometries. Due to differing experimental techniques, the goal of this effort is to provide a consistent perspective on the possibility of anisotropic porous materials for drag reduction by conducting pressure drop measurements for a range of geometries previously used in the literature and two completely novel geometries.

Using the same cubic geometry as Vijay et al. (2023), skin friction profiles and permeability ratios for Reynolds number [500, 3000] were reproduced illustrating consistency in the experimental procedure, setup, and results. Using the trapezoidal riblet geometry utilized in the paper by Morimoto (2022), skin friction coefficient measurements below the smooth plate were not observed. This is consistent with the conclusions from Morimoto's analysis that utilized Reynolds shear stress measurements as opposed to direct pressure drop measurements. The two novel geometries, elliptical and gyroid, tested also did not result in drag reduction despite demonstrating streamwise preferential permeability.

The lack of drag reduction for the highly anisotropic structures seemingly contradicts the results from Gomez and Garcia (2019). However, there are two important caveats that necessitate further experimental research and discussion. Based on the computational studies by Gomez and Garcia, the key factor in the reduction of drag is ϕ_{xy} under the condition that $K_{yy} = K_{zz}$. It is evident that for more complex structured geometries (i.e. trapezoidal and gyroid) the symmetry condition is not met, obscuring the relationship between anisotropy (ϕ_{xy}) and drag reduction at the Reynolds numbers tested. Furthermore, it is possible that the decreasing trend noted in the friction factor profiles extends to higher Reynolds numbers. This allows for structures with higher anisotropy to potentially result in even lower friction factors than those recorded. From previous research, it is expected that the friction factor asymptotically reaches a lower bound at Reynolds numbers >4000. Therefore, experiments for Reynolds numbers >3000 need to be conducted to clarify the relationship between anisotropy and friction factor.

Based on the results from this report, two avenues of further experimentation emerge. First, experiments with greater Reynolds numbers need to be conducted to characterize the

friction coefficient profile. Due to the ability of the gyroid and riblet geometries to reduce KH vortices along the wall-normal direction, a geometric parameter sweep increasing the pore sizing in the streamwise directions should be conducted. These experiments will illuminate more clearly whether the symmetry condition $\phi_{xy} = \phi_{xz}$ is plausible for more complex geometries and whether this criterion is conducive to drag reduction as expected from computational experiments.

Appendix

Uncertainty Analysis for the Permeability

Each of the permeability plots had coefficients proportional to the bulk velocity of the flow which is expected based on Darcy's equation. However, each of these values has an uncertainty that can be represented by the R^2 value. The figure below illustrates how the slope is determined from the plot and how the R^2 value is used to represent its uncertainty.

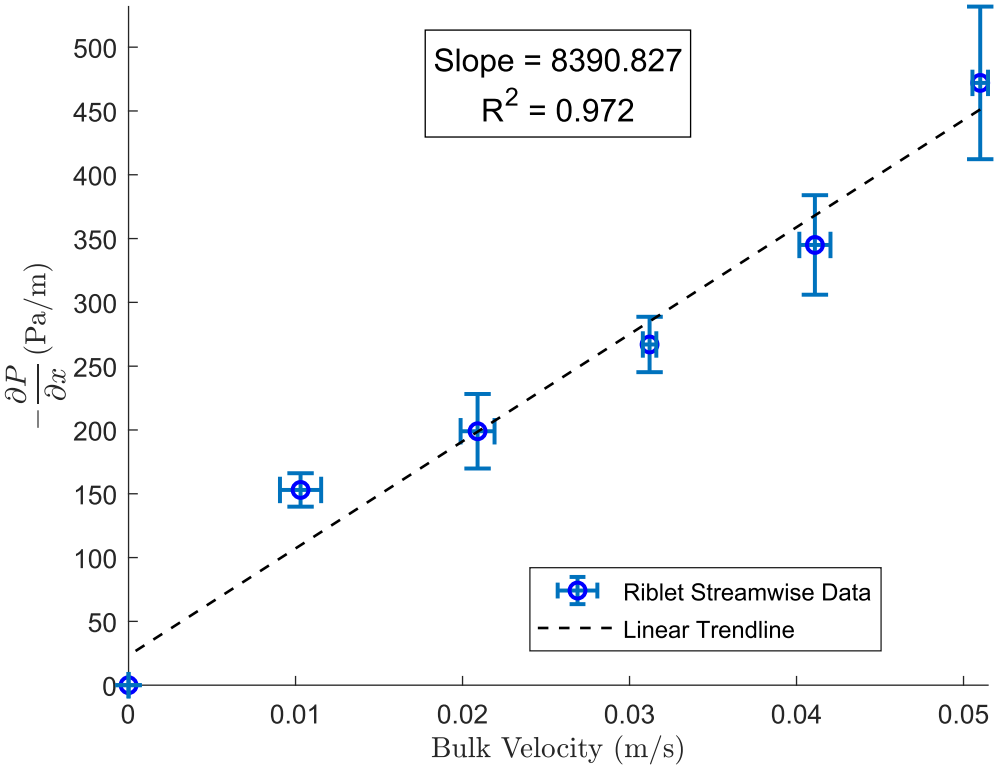

The equation that relates R^2 to the percent uncertainty is found from equation 6.

$$\% = \sqrt{\frac{\frac{1}{R^2} - 1}{n - 2}} \qquad \text{Equation 7}$$

where n is the number of points. Conceptually this equation makes sense because as R^2 decreases the uncertainty between the relationship between bulk velocity and the pressure gradient increases. In addition, when the R^2 value is equal to one, the uncertainty is zero.

Updated Cost Estimate

AME-441 Group 26 - Cost Estimate

Experiments on the Permeability of Anisotropic Porous Structures for Drag Reduction

as of 12/10/2024

	Vendor/Manufacturer	Model/Part No.	Qty.	Unit Price	Item Price
EXPENSES FOR ITEMS AVAILABLE IN LAB					
Equipment					
USB Multifunction DAQ	National Instruments	USB-6211	1	$792.00	$792.00
Benchtop Water Channel	University of Southern California	Custom	1	$5,000.00	$5,000.00
Benchtop Permeameter Setup	University of Southern California	Custom	1	$1,250.00	$1,250.00
Materials					
High Resolution Differential Pressure Transducer	Omega Inc.	PX-409	1	$1,099.88	$1,099.88
2-20 GPM Flowmeter	Blue-White Industries	RB-100PI-GPM2	1	$379.99	$379.99
1/2" Full Port Ball Valve	TJ Valve	SS316BV050FPX	1	$19.99	$19.99
Submersible Pump	Little Giant	503103	1	$250.50	$250.50
Electronic Proportioning Valve	Omega Inc.	PV14-SS	1	$1,807.91	$1,807.91
1/2" Clear Silicone Tubing (5' L)	Grainger	ZUSA-HT-3211	2	$14.54	$29.08
				Sub-total Cost:	**$10,629.35**
EXPENSES FOR ITEMS REQUIRED FOR PURCHASE					
Manufacturing					
Clear Resin V4 (Form 3)	Formlabs	RS-F2-GPCL-04	2	$149.00	$298.00
PT Tubing	Grainger	3902N295	10 ft	$0.88/ft	$8.80
Brushes	Amazon	B087NHNYPN	1	$6.99	$6.99
Scotch Bright Non Scratch Scour Pad	Target	403R56	2	$6.99	$13.98
	Scotch Brite	50051141328664.00	2	$6.99	$13.98
BUDGET					
AME-441 project budget ($100 per student)				***Sub-total Cost:***	**$341.75**
				TOTAL PROJECT EXPENSES:	**$10,971.10**
			4	$100.00	$400.00
				TOTAL BUDGET:	**$400.00**

Updated GANNT Chart

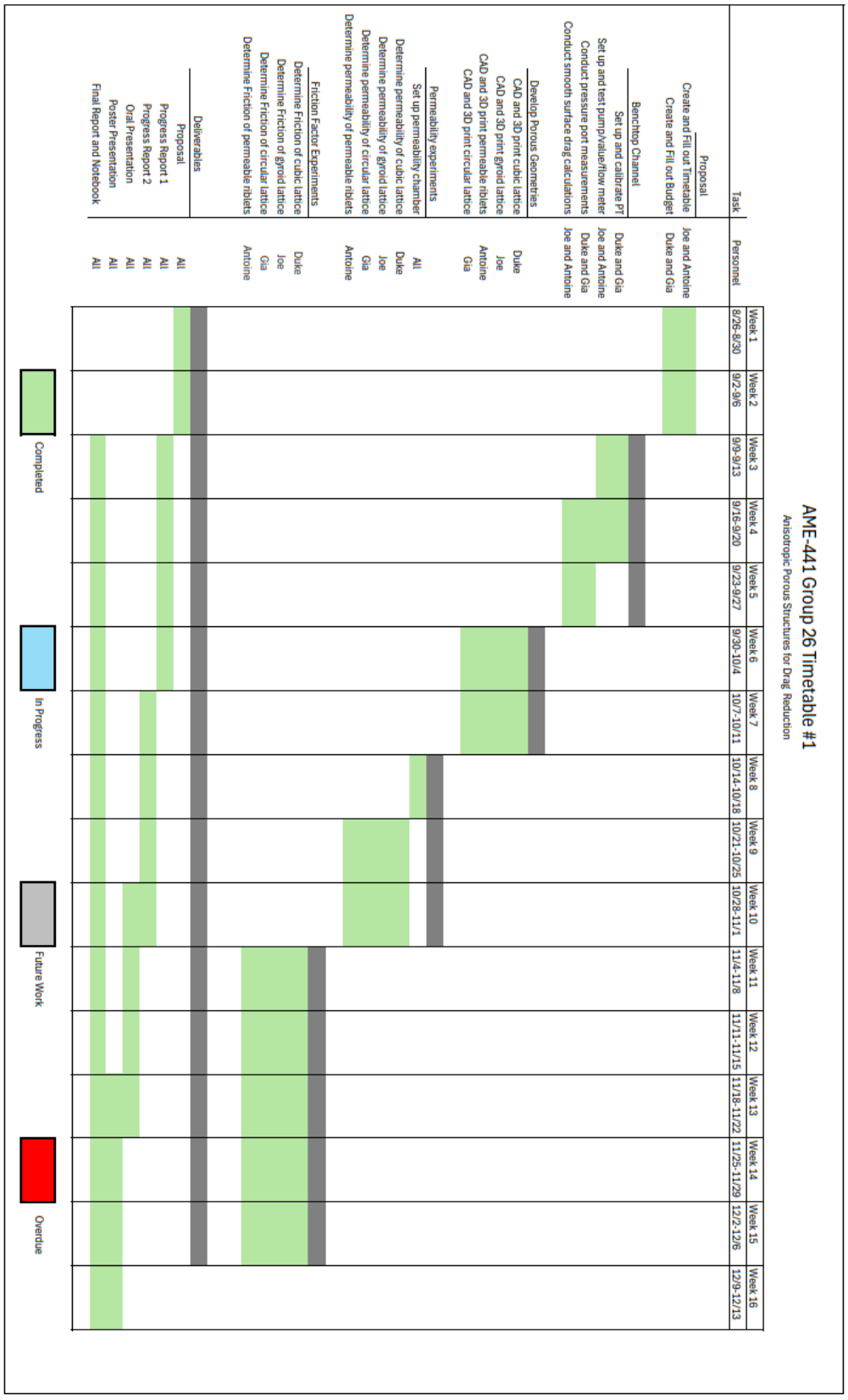

Works Cited

F. Zhao, Y. Xiong, K. Ito, B. Rietbergen, and S. Hofmann, “Porous Geometry Guided Micro-mechanical Environment Within Scaffolds for Cell Mechanobiology Study in Bone Tissue Engineering,” Available: https://www.ncbi.nlm.nih.gov/pmc/articles/PMC8476750/

G. Gomez-de-Segura, and R. Garcia-Mayoral, “Turbulent drag reduction by anisotropic permeable substrates - analysis and direct numerical simulations.” Available: https://link.springer.com/article/10.1007/s10494-018-9916-4

Gavrilakis, S.: Post-transitional periodic flow in a straight square duct. J. Fluid Mech. 859, 731–753 (2019). https://doi.org/10.1017/jfm.2018.811

M. Morimoto, Y. Kuwata, and K. Suga. "Discussion on the possibility of turbulent drag reduction by streamwise preferential porous medium” European Research Community on Flow, Turbulence and Combustion (ERCOFTAC), 2022. Available: https://omu.repo.nii.ac.jp/record/2000388/files/2023000360.pdf

M. Morimoto, R. Aoki, Y. Kuwata & K. Suga,“Measurements for Characteristics of Turbulence over a Streamwise Preferential Porous Substrate,” Available: https://link.springer.com/article/10.1007/s10494-023-00493-4

Mubarak, A.K., and P.S. Tide. *Bonfring*, conference.bonfring.org/papers/gct_icmf2013/icmf234.pdf. Accessed 1 Dec. 2024.

N.-S. Cheng. Formulas for friction factor in transitional regimes. Journal of Hydraulic Engineering, 134(9):1357–1362, 2008.

Omega, “Omega high accuracy pressure transducers,” Available: https://assets.omega.com/pdf/test-and-measurement-equipment/pressure/pressure-transducers/PX409_Series.pdf (accessed Dec. 8, 2024).

P. Ricco, M. Skote, M. A. Leschziner, “A review of turbulent skin-friction drag reduction by near-wall transverse forcing,” Available: https://www.sciencedirect.com/science/article/abs/pii/S037604212100018X.

S. Vijay, and M. Luhar, “Pressure Drop Measurements over Anisotropic Porous Substrates in Channel Flow.” Available: https://meetings.aps.org/Meeting/DFD23/Session/J25.9

Y. F. Fu, C.Q. Yuan, X.Q. Bai,“Marine drag reduction of shark skin inspired riblet surfaces,” Available: https://www.sciencedirect.com/science/article/pii/S2405451816300484